LETTERS
PUBLISHED ONLINE: 18 JULY 2016 | DOI: 10.1038/NGEO2767
nature geoscience

Reorganization of the North Atlantic Oscillation during early Holocene deglaciation

Jasper A. Wassenburg[1,2*], Stephan Dietrich[3,4], Jan Fietzke[5], Jens Fohlmeister[6], Klaus Peter Jochum[7], Denis Scholz[2], Detlev K. Richter[1], Abdellah Sabaoui[8], Christoph Spötl[9], Gerrit Lohmann[4], Meinrat O. Andreae[10] and Adrian Immenhauser[1]

The North Atlantic Oscillation is the dominant atmospheric pressure mode in the North Atlantic region and affects winter temperature and precipitation in the Mediterranean, northwest Europe, Greenland, and Asia[1]. The index[1] that describes the sea-level pressure difference between Iceland and the Azores is correlated with a dipole precipitation pattern over northwest Europe and northwest Africa. How the North Atlantic Oscillation will develop as the Greenland ice sheet melts is unclear[2]. A potential past analogue is the early Holocene, during which melting ice sheets around the North Atlantic[3,4] freshened surface waters, affecting the strength of the meridional overturning circulation[5]. Here we present a Holocene rainfall record from northwest Africa based on speleothem $\delta^{18}O$ and compare it against a speleothem-based rainfall record from Europe[6]. The two records are positively correlated during the early Holocene, followed by a shift to an anti-correlation, similar to the modern record, during the mid-Holocene. On the basis of our simulations with an Earth system model, we suggest the shift to the anti-correlation reflects a large-scale atmospheric and oceanic reorganization in response to the demise of the Laurentide ice sheet and a strong reduction of meltwater flux to the North Atlantic, pointing to a potential sensitivity of the North Atlantic Oscillation to the melting of ice sheets.

The variability of the North Atlantic Oscillation (NAO) has severe socio-economic and ecological consequences[7], as it affects climate on interannual to multi-decadal timescales[1]. However, long-term NAO reconstructions based on proxy data also indicate large variability on centennial to millennial timescales[8,9]. To assess the NAO behaviour in the context of potential ice-sheet melting as a result of anthropogenic warming[10], robust proxy data on the NAO variability during the demise of the large Northern Hemisphere ice sheets during the early-to-mid-Holocene[3,4] (11.5–6.8 ka, thousand years before AD 1950) are particularly informative.

The NAO can be described by the sea-level pressure (SLP) difference between the Icelandic Low and the Azores High[1], but also exhibits non-stationary behaviour[11,12], which is related to latitudinal or longitudinal shifts of the NAO SLP centres (that is, the Icelandic Low and the Azores High) that cause changes in the NAO angle index[11]. This has a large impact on the position or orientation of the NAO/rainfall correlation belts (Fig. 1), and thus affects NAO teleconnection patterns in the North Atlantic/European area. Although there is evidence that the NAO operated throughout the Holocene[13], the longest NAO reconstruction, derived from a lake record from West Greenland[9], extends only back to 5.2 ka. This calls for palaeoclimate reconstructions from key NAO regions covering the entire Holocene.

Here we present a high-resolution (15 ± 11 years), precisely dated speleothem $\delta^{18}O$ rainfall record from Grotte de Piste[14] in northwest Morocco (Fig. 1), which covers the early-to-late-Holocene (stalagmite GP2; Fig. 2 and Supplementary Figs 4–6 and Supplementary Table 1). Northwest Morocco is a key NAO region (Fig. 1 and Supplementary Fig. 2) and has a highly seasonal climate with wet winters and dry summers. Speleothem rainfall records from northwest Morocco are, thus, dominated by winter rainfall variability, which is the season with the largest influence of the NAO (ref. 1). We compare the northwest Moroccan record against a speleothem-based rainfall proxy record from Bunker Cave, western Germany[6], another NAO-sensitive region (Supplementary Text and Supplementary Fig. 2 and Supplementary Table 4). A comparison of the northwest Moroccan and western German rainfall records with other proxy records from NAO-influenced regions (Fig. 1a,b and Supplementary Fig. 11) shows that both cave sites recorded NAO variability during the mid-to-late-Holocene. This increases the confidence that both records were also linked to NAO variability during the early Holocene.

At present, winter rainfall amounts in northwest Morocco and western Germany are negatively correlated (Fig. 1). However, the western German site is located on the southern border of the northern NAO/rainfall correlation belt (Fig. 1b) and is thus sensitive to latitudinal and/or longitudinal shifts of the NAO SLP centres, rendering it useful for studying the non-stationary behaviour of the NAO.

On the basis of the northwest Moroccan record, NAO-like conditions fluctuated between relatively positive modes, centred around 11.2, 10.7, 9.9, 8.5, 8.0, 7.6, 6.9, 6.5, 6.0, 5.6, 5.0, 3.4 and 2.8 ka, and relatively negative modes (Fig. 2). Furthermore, the GP2 $\delta^{18}O$ record and the Bunker Cave Mg/Ca record (Fig. 2)

[1]Institute of Geology, Mineralogy, and Geophysics, Ruhr University Bochum, Universitätsstrasse 150, 44801 Bochum, Germany. [2]Institute for Geosciences, University of Mainz, Johann-Joachim-Becher-Weg 21, 55128 Mainz, Germany. [3]Federal Institute for Hydrology, 56068 Koblenz, Germany. [4]Alfred Wegener Institute Helmholtz Centre for Polar and Marine Research, 27570 Bremerhaven, Germany. [5]Helmholtz Centre for Ocean Research Kiel (GEOMAR), Wischhofstrasse 1-3, 24148 Kiel, Germany. [6]Institute for Environmental Physics, University of Heidelberg, Im Neuenheimer Feld 229, 69120 Heidelberg, Germany. [7]Climate Geochemistry and Biogeochemistry Departments, Max Planck Institute for Chemistry, PO Box 3060, 55020 Mainz, Germany. [8]Faculty of Sciences Dhar Mahraz, BP 1796 Atlas, Fès, Morocco. [9]Institute of Geology, University of Innsbruck, Innrain 52, 6020 Innsbruck, Austria. [10]Biogeochemistry Department, Max Planck Institute for Chemistry, PO Box 3060, 55020 Mainz, Germany. *e-mail: jasper.wassenburg@rub.de

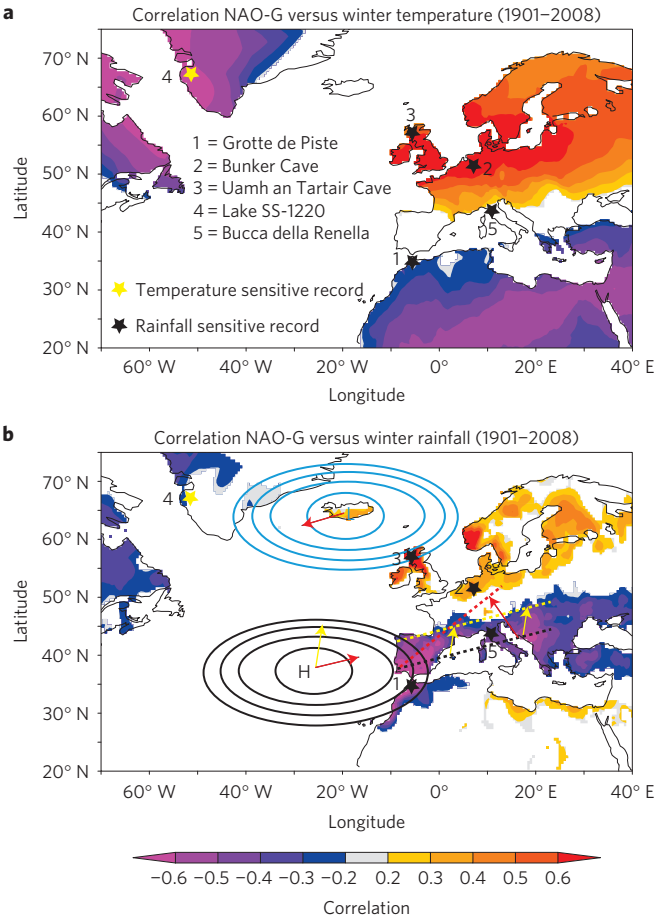

Figure 1 | Correlations between the NAO index and winter climate parameters. a, NAO-G index[23] versus winter surface-air temperature[24]. The climate records discussed in the text and the supplement are indicated: (1) northwest Morocco (ref. 25, this study), (2) western Germany[6], (3) northwest Scotland[26], (4) west Greenland[9], (5) western Italy[27]. **b**, NAO-G index versus winter rainfall[23], with the potential movements of the southern NAO-precipitation correlation belt under the influence of changing positions of the Icelandic Low/Azores High pressure centres indicated. A southwestward shift of the Icelandic Low relative to the Azores High would lead to a strong negative NAO angle index[11].

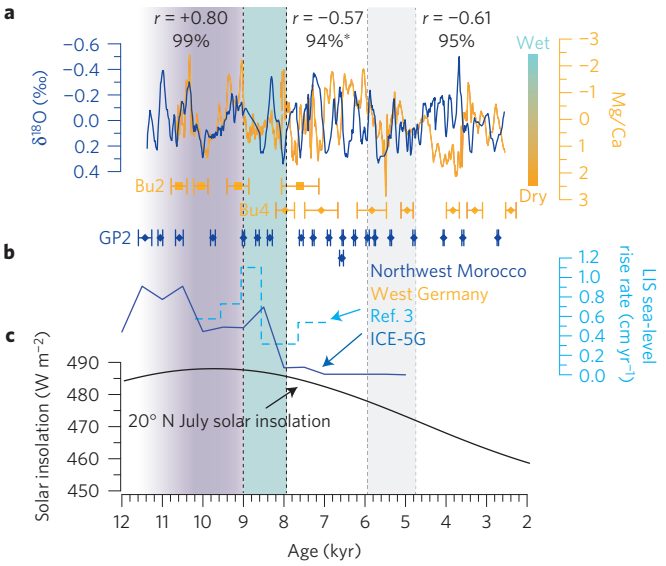

Figure 2 | Comparison of rainfall variability between northwest Morocco and western Germany during the early-to-mid-Holocene. a, GP2 $\delta^{18}O$ record (blue; detrended) and the Bu2 and Bu4 Mg/Ca records[6], normalized to their mean and tuned to GP2 $\delta^{18}O$ (yellow); using five-point running mean data. Correlation indicated by shading: white (negative), violet (positive) and grey (not significant). Dating uncertainties: squares (Bu2) and diamonds (Bu4, GP2). The turquoise box indicates the transition zone. **b**, Contribution of the Laurentide ice sheet to sea-level rise according to ref. 3 (light blue) and the ICE-5G model[4] (dark blue). **c**, Orbital forcing of July solar insolation for 20° N (ref. 28).

show significant negative correlations for the early mid-Holocene (8.1–5.9 ka; $r = -0.57$, 94%) and the late Holocene (4.7–2.5 ka; $r = -0.61$, 95%; Supplementary Table 2).

During the periods dominated by negative correlations, the NAO was probably in its 'modern' state (that is, warm/wet winter conditions in western Germany correspond to dry conditions in northwest Morocco). The 5.9–4.7 ka period does not show a significant correlation, and is therefore not discussed further (see Methods). However, during the early Holocene, we observe a significant positive correlation between the two records (10.7–9.0 ka; $r = +0.80$, 99%). Consequently, a transition from a positive to a negative correlation on millennial timescales must have occurred from the early Holocene to the mid-Holocene, which appears to coincide with a strong decrease in the contribution of melt water from the Laurentide ice sheet to global sea-level rise[3] (Fig. 2b). The timing and duration of the transition remain uncertain due to the uncertainties of the age models and the applied tuning approach (Fig. 2; also see Supplementary Text and Supplementary Figs 8–10). We hypothesize that the early Holocene positive correlation might reflect a modulated NAO-like SLP pattern induced either by a more northwardly positioned Icelandic Low and/or Azores High, shifting the westerlies in the same direction (Fig. 1b), or a more eastwardly (westwardly) positioned Azores High (Icelandic Low; Fig. 1b), inducing increasingly southwesterly wind directions[11]. These potential shifts may be related to changes in the mean state of the SLP field that cause the NAO centres of SLP to shift as well.

During the early Holocene, orbital forcing of insolation (Fig. 2c) could have played a role by shifting the Hadley cell circulation and its components, the Inter Tropical Convergence Zone (ITCZ) and the Azores High, northwards. However, it is well known that the northerly position of the ITCZ caused the African humid period, which lasted until about 5 ka (ref. 15). Thus, this does not explain the shift to a negative correlation between the two proxy records around 8.4 ka. To investigate this further, we examined climate simulations performed with the fully coupled Earth system model COSMOS (ref. 16), using late Holocene (pre-industrial; PI), mid-Holocene (6k) and early Holocene (9k) boundary conditions[17] (Supplementary Table 3). Because the early Holocene was characterized by the final disappearance of the Laurentide ice sheet[3,4] (Fig. 2b), we performed three additional climate simulations to distinguish between the potential effects of the presence of the Laurentide ice sheet (that is, its topography and high albedo), its melt water contribution, and nonlinear effects due to a combination of all early Holocene features (9k.ice, 9k.melt and 9k.comb, respectively). The simulation 9k.comb resembles the early Holocene conditions most realistically. The spatial resolution of the models (approximately 3.75° × 3.75°) limits the accuracy with which local precipitation can be simulated. Therefore, correlations between local precipitation at Grotte de Piste and Bunker Cave do not show any significant differences (Supplementary Fig. 12). However, changes on multi-decadal timescales in large-scale atmospheric circulation patterns associated with local precipitation, which are the focus of this study, can be reliably modelled.

Figure 3a,b and Supplementary Figs 13 and 14 show that only the 9k.comb simulation indicates a latitudinal/longitudinal shift of the

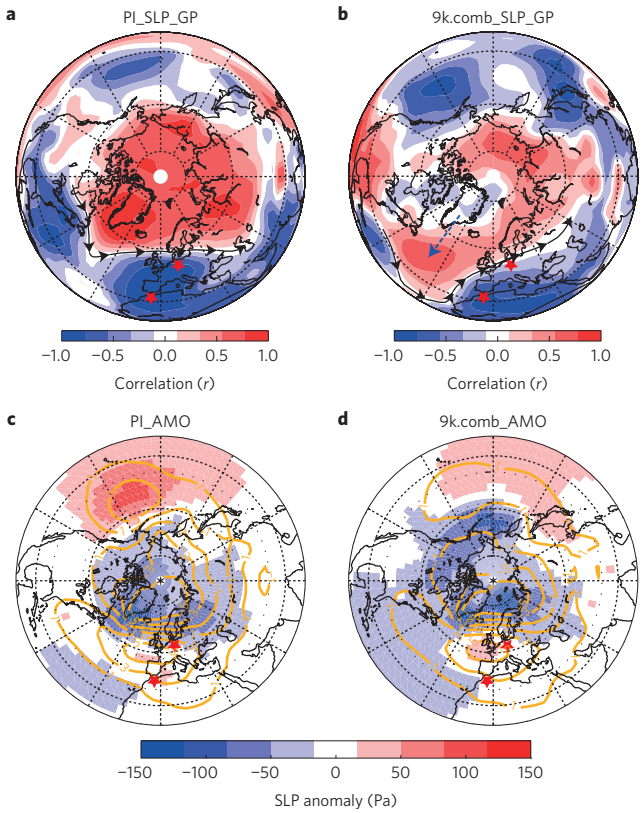

Figure 3 | Results of the COSMOS climate simulations. a, Pre-industrial (PI) climate simulation. Correlations between 21-year running mean sea-level pressure (SLP) and 21-year running mean local precipitation at Grotte de Piste for the winter season (December–February). Main atmospheric circulation patterns are indicated by the black arrows. **b**, Same as **a**, but for the 9k.comb early Holocene climate simulation. The blue arrow indicates the southwestward shift of the Icelandic Low. **c**, AMO SLP anomaly (colour coded) versus NAO SLP fields (yellow contour lines) for PI climate simulation. **d**, Same as **c**, but for the 9k.comb climate simulation.

Icelandic Low and Azores High. In particular, northwest Moroccan precipitation was related to a modulated NAO-like SLP field that is characterized by a strong negative angle index[11] dominated by southwesterly winds, which can also bring moisture to western Germany. These shifts confirm our hypothesis. In addition, the position of the Azores High associated with precipitation in western Germany has a more northerly position in the 9k.comb simulation (Fig. 3c,d and Supplementary Fig. 16). Both shifts affect the position of the southern NAO/rainfall correlation belt (Fig. 1), forcing northwest Morocco and western Germany into the same hydrological regime. We emphasize that these shifts are visible only in the 9k.comb simulations, which points to a combined effect of the presence of the Laurentide ice sheet and its meltwater. A possible mechanism that could explain these shifts involves changes in sea surface temperature (SST), which produce changes in surface heat flux associated with anomalous SLP patterns[18].

To investigate the dominance of North Atlantic SST on winter SLP, we performed a Canonical Correlation Analysis (CCA, see Methods). The CCA indicates that, during pre-industrial conditions, a tripolar NAO-like SST pattern driven by turbulent atmospheric energy flux[19] dominates, whereas in the 9k.comb simulation, ocean-driven Atlantic Multi-decadal Oscillation (AMO; ref. 20)-like patterns dominate (Supplementary Fig. 15). The AMO has been considered as a dominant mode of variability in North Atlantic SST, with typical frequencies between 55 and 80 years[20] throughout the Holocene[17,21], but also on centennial to millennial timescales[22]. Because climate simulations indicated that the AMO was more pronounced during the early Holocene compared to the mid to late Holocene[17] due to the combined effect of the Laurentide ice sheet and its meltwater, the AMO may have been an important factor in modifying NAO SLP fields during the early Holocene.

To assess whether the AMO is able to modulate NAO SLP fields on multi-decadal timescales, we plotted SLP anomalies for positive minus negative AMO indices together with NAO SLP contours. The strongest potential NAO modulation can be seen in the PI and the 9k.comb simulations, with negative SLP anomalies located west of Iceland, close to the Icelandic Low (Fig. 3c,d and Supplementary Fig. 16). For the 9k.comb simulation, an additional negative SLP anomaly is located north of Scandinavia, which falls within the centre of the modelled northern NAO SLP centre. Furthermore, a positive SLP anomaly is located within the southern NAO SLP centre. Therefore, the AMO may have affected the strength of the Icelandic Low and the Azores High during the early Holocene. In addition, the SLP anomaly west of Iceland may have caused changes in the longitudinal position of the Icelandic Low, modifying the westerly wind direction (Fig. 1). However, the AMO does not directly explain the shift in the Icelandic Low associated with northwest Moroccan precipitation (Fig. 3a,b). Nevertheless, it is likely that the AMO modulated the early Holocene NAO SLP fields and may have affected NAO teleconnection patterns.

We suggest that the mean state of the North Atlantic SLP field changed from the early to the mid-Holocene in response to the deglaciation of the Laurentide ice sheet, which affected the longitudinal and latitudinal positions of the NAO SLP centres. We also show that, during the early Holocene, the NAO SLP field may have been further modulated by the more pronounced AMO. Therefore, NAO teleconnection patterns were different from the pre-industrial era, which explains the observed shift from a positive to a negative correlation between local precipitation at northwest Morocco and western Germany. As a consequence, northwest Morocco and western Germany were located in the same hydrological regime during the early Holocene.

Most importantly, our analysis clearly shows that the NAO teleconnection patterns were affected by a nonlinear climate response to the presence of the Laurentide ice sheet and its meltwater. Although it remains difficult to foresee how the predicted future melting of the Greenland ice sheet[2] may affect the NAO and its interaction with climate modes on longer timescales (that is, the AMO), our results indicate that the response will primarily depend on the amount of melt water and the rate of melting[3].

Methods

Methods, including statements of data availability and any associated accession codes and references, are available in the online version of this paper.

Received 19 April 2016; accepted 15 June 2016; published online 18 July 2016

References

1. Hurrell, J. W. Decadal trends in the North-Atlantic Oscillation—regional temperatures and precipitation. *Science* **269,** 676–679 (1995).
2. IPCC *Climate Change 2013: The Physical Science Basis* (eds Stocker, T. F. *et al.*) (Cambridge Univ. Press, 2013).
3. Carlson, A. E. *et al*. Rapid early Holocene deglaciation of the Laurentide ice sheet. *Nature Geosci.* **1,** 620–624 (2008).
4. Peltier, W. R. Global glacial isostasy and the surface of the ice-age Earth: the ICE-5G (VM2) model and GRACE. *Annu. Rev. Earth Planet. Sci.* **32,** 111–149 (2004).
5. LeGrande, A. N. *et al*. Consistent simulation of multiple proxy responses to an abrupt climate change event. *Proc. Natl Acad. Sci. USA* **103,** 837–842 (2006).
6. Fohlmeister, J. *et al*. Bunker Cave stalagmites: an archive for central European Holocene climate variability. *Clim. Past* **8,** 1751–1764 (2012).

7. Vicente Serrano, S. M. & Trigo, R. M. *Hydrological, Socioeconomic and Ecological Impacts of the North Atlantic Oscillation in the Mediterranean Region* Vol. 46 (Advances in Global Change Research, Springer, 2011).
8. Trouet, V. *et al*. Persistent positive North Atlantic Oscillation mode dominated the Medieval Climate Anomaly. *Science* **324,** 78–80 (2009).
9. Olsen, J., Anderson, J. N. & Knudsen, M. F. Variability of the North Atlantic Oscillation over the past 5,200 years. *Nature Geosci.* **5,** 808–812 (2012).
10. Dong, B. W., Sutton, R. T. & Woollings, T. Changes of interannual NAO variability in response to greenhouse gases forcing. *Clim. Dynam.* **37,** 1621–1641 (2011).
11. Wang, Y. H., Magnusdottir, G., Stern, H., Tian, X. & Yu, Y. Decadal variability of the NAO: introducing an augmented NAO index. *Geophys. Res. Lett.* **39,** L21702 (2012).
12. Ortega, P. *et al*. A model-tested North Atlantic Oscillation reconstruction for the past millennium. *Nature* **523,** 71–74 (2015).
13. Rimbu, N., Lohmann, G., Lorenz, S. J., Kim, J. H. & Schneider, R. R. Holocene climate variability as derived from alkenone sea surface temperature and coupled ocean–atmosphere model experiments. *Clim. Dynam.* **23,** 215–227 (2004).
14. Wassenburg, J. A. *et al*. Climate and cave control on Pleistocene/Holocene calcite-to-aragonite transitions in speleothems from Morocco: elemental and isotopic evidence. *Geochim. Cosmochim. Acta* **92,** 23–47 (2012).
15. deMenocal, P. *et al*. Abrupt onset and termination of the African Humid Period: rapid climate responses to gradual insolation forcing. *Quat. Sci. Rev.* **19,** 347–361 (2000).
16. Jungclaus, J. H. *et al*. Climate and carbon-cycle variability over the last millennium. *Clim. Past* **6,** 723–737 (2010).
17. Wei, W. & Lohmann, G. Simulated Atlantic multidecadal oscillation during the Holocene. *J. Clim.* **25,** 6989–7002 (2012).
18. Czaja, A. & Frankignoul, C. Influence of the North Atlantic SST on the atmospheric circulation. *Geophys. Res. Lett.* **26,** 2969–2972 (1999).
19. Deser, C., Alexander, M. A., Xie, S. P. & Phillips, A. S. Sea surface temperature variability: patterns and mechanisms. *Annu. Rev. Mar. Sci.* **2,** 115–143 (2010).
20. Delworth, T. L. & Mann, M. E. Observed and simulated multidecadal variability in the Northern Hemisphere. *Clim. Dynam.* **16,** 661–676 (2000).
21. Knudsen, M. F., Seidenkrantz, M. S., Jacobsen, B. H. & Kuijpers, A. Tracking the Atlantic Multidecadal Oscillation through the last 8,000 years. *Nature Commun.* **2,** 178 (2011).
22. Oglesby, R., Feng, S., Hu, Q. & Rowe, C. The role of the Atlantic Multidecadal Oscillation on medieval drought in North America: synthesizing results from proxy data and climate models. *Glob. Planet. Change* **84–85,** 56–65 (2012).
23. Jones, P. D., Jonsson, T. & Wheeler, D. Extension to the North Atlantic Oscillation using early instrumental pressure observations from Gibraltar and south-west Iceland. *Int. J. Climatol.* **17,** 1433–1450 (1997).
24. Harris, I., Jones, P. D., Osborn, T. J. & Lister, D. H. Updated high-resolution grids of monthly climatic observations—the CRU TS3.10 Dataset. *Int. J. Climatol.* **34,** 623–643 (2014).
25. Wassenburg, J. A. *et al*. Moroccan speleothem and tree ring records suggest a variable positive state of the North Atlantic Oscillation during the Medieval Warm Period. *Earth Planet. Sci. Lett.* **375,** 291–302 (2013).
26. Proctor, C. J., Baker, A. & Barnes, W. L. A three thousand year record of North Atlantic climate. *Clim. Dynam.* **19,** 449–454 (2002).
27. Drysdale, R. *et al*. Late Holocene drought responsible for the collapse of Old World civilizations is recorded in an Italian cave flowstone. *Geology* **34,** 101–104 (2006).
28. Laskar, J. *et al*. A long-term numerical solution for the insolation quantities of the Earth. *Astron. Astrophys.* **428,** 261–285 (2004).

Acknowledgements

This work was funded by the Deutsche Forschungsgemeinschaft (DFG; project IM 44/1, and WA3532/1-1) and the Max Planck Society. We would like to thank W. Wei for providing model output and performing the CCA-analysis and acknowledge D. Fleitmann for fruitful discussions. The staffs in the isotope laboratories at Bochum and Mainz (U. Weis, B. Stoll, A. Niedermayr, D. Buhl, B. Gehnen, U. Schulte) are acknowledged for their help with sample preparation and measurements. In addition, T. Reinecke, the thin section lab at Bochum and our local speleo-guides E. H. El Mansouri and T. Echchibi are gratefully acknowledged. A. Fink (Institute for Geophysics and Meteorology, University of Cologne) is thanked for providing rainfall data from the weather station in Taza, Morocco.

Author contributions

J.A.W. wrote the paper and prepared and performed the stable isotope and trace element analysis; J.A.W., S.D., A.I. and D.K.R., were involved in the study design; S.D., and G.L. analysed the climate modelling data; J.A.W. and D.S. were involved in the age–depth modelling; J.A.W., J.Fohlmeister and D.S. were involved in the speleothem data interpretation; S.D., G.L. and J.A.W. contributed to the climate discussion; J.Fietzke performed the ^{230}Th/U dating of stalagmite GP2; J.Fohlmeister performed the tuning and correlation analysis; C.S. performed the δ^{18}O analysis of the rainwater samples; K.P.J. provided support with trace element analysis; M.O.A. provided essential feedback to multiple draft versions of the manuscript; A.S. provided logistical support essential for the collection of stalagmite GP2. All authors discussed the results and provided comments on the manuscripts.

Additional information

Supplementary information is available in the online version of the paper. Reprints and permissions information is available online at www.nature.com/reprints. Correspondence and requests for materials should be addressed to J.A.W.

Competing financial interests

The authors declare no competing financial interests.

Methods

Stalagmite GP2. Stalagmite GP2 was part of a column and was sampled in 2009 in Grotte de Piste. It contains a 601-mm-long Holocene part dated by 20 ^{230}Th/U ages (Supplementary Table 1 and Supplementary Fig. 4). Carbon and oxygen isotopes were measured at an average resolution of 15 yr (±11 yr), and trace elements were analysed for Sr, P, Y and U concentrations at the same resolution to corroborate the interpretation of the δ^{18}O record. This multi-proxy approach provides solid evidence that the (multi-) centennial trends in the GP2 δ^{18}O record represent past rainfall variability—that is, higher δ^{18}O values reflect drier conditions and vice versa (Supplementary Figs 5 and 6). To examine (multi-) centennial timescale patterns, we have detrended the GP2 δ^{18}O and δ^{13}C records (Supplementary Fig. 6). A detailed description of stalagmite GP2 and the interpretation of the proxy data are given in the Supplementary Text and Supplementary Figs 4–6.

Carbonate carbon and oxygen isotope analysis. Carbon and oxygen isotope analyses were performed at the Ruhr University Bochum (RUB), Germany, with a Gasbench coupled to a Finnigan MAT 253 isotope ratio mass spectrometer. For sampling at a resolution of 1 mm (the equivalent of 15 ± 11 yr), a hand-held (Dremel) tool equipped with a flat-tipped, 0.5-mm-diameter dentist drill was used. Carbon and oxygen isotope values are expressed in ‰ with respect to the Vienna PDB (VPDB) standard. Sample aliquots weighing between 0.27 and 0.33 mg were dried for 48 h in an oven at 105 °C. To avoid atmospheric contamination, the vials were flushed with He, after which phosphoric acid (104%) was added to the sample. CO1 and CO8 carbonate standards were used for calibration, and quality control was assessed by using the NBS19 and the RUB internal carbonate standards. For every sample batch of 48 samples, four duplicates were analysed to check for sample homogeneity. Adding the averaged internal standard deviations derived from the analysis of nine peaks per sample to the averaged difference of each duplicate suggests a precision of ±0.12‰ for δ^{13}C and ±0.14‰ for δ^{18}O.

Due to the different isotope fractionation, calcite is 0.8‰ lower in δ^{18}O (ref. 29) and 1.7‰ lower in δ^{13}C (ref. 30) compared to aragonite when precipitated from a fluid with the same isotopic composition. Therefore, we corrected calcite values at the base of the Holocene transect by adding 0.8‰ for δ^{18}O and 1.7‰ for δ^{13}C to compare them to the aragonite values.

δ^{18}O analysis in rainwater samples. Rainwater samples were collected on a daily basis from August 2010 to November 2011. Data presented here represent event samples (August 2010 to February 2011) and monthly samples (March to November 2011). Samples were collected in a collection vessel through a funnel with a small 5-mm-diameter entrance to minimize evaporation effects. Samples were prepared at the University of Innsbruck, Austria, using the CO_2 equilibration technique, and analysed using a Gasbench II interfaced with a Delta^{Plus}XL isotope ratio mass spectrometer. Calibration of the mass spectrometer was accomplished using VSMOW, GISP and SLAP standards. The long-term 1-sigma analytical precision of the δ^{18}O values is 0.08‰.

Trace element analysis. Phosphorous, Sr, Y and U abundances were determined by laser ablation inductively coupled plasma mass spectrometer (LA-ICP-MS) with a Thermo Finnigan Element 2 ICP-MS and a New Wave UP213 laser at the Max Planck Institute for Chemistry, Mainz, Germany. The isotopes 31, 86, 89 and 238, respectively, were used for analysis. Samples were ablated with an energy density of 15.7 J cm^{-2} at 1 mm resolution (the equivalent of 15 ± 11 yr). A relatively large round, 100-µm-diameter spot was used for all measurements to average out heterogeneities within a given growth increment[31,32]. The first two to five scans of every single spot analysis were discarded, to avoid any effect of surface contamination. Total measurement time per spot analysis was between 100 and 105 s. Intensities (counts per second) were corrected for background noise. The NIST SRM 612 glass reference material and the MACS3 and MACS1 carbonate reference materials were measured 9–15 times equally distributed in the sequence in blocks of three individual spot analyses. Absolute concentrations were derived by using ^{43}Ca as an internal standard and calculating an averaged relative sensitivity factor[33] based on the NIST SRM 612 (85,050 ppm Ca) and MACS3 (376,900 ppm Ca) reference materials using the most recent reference values[34]. MACS1 elemental concentrations were used as a quality control.

Measurement uncertainties are between 5 and 15% (20% for very low P abundances <4 ppm), as demonstrated by ref. 32, which focused on LA-ICP-MS analysis on carbonates including speleothems. Detection limits for P, Sr, Y and U are 4, 0.5, 0.01 and 0.0002 ppm, respectively[32], although they may be a factor of three to four smaller for P and Y, depending on measurement conditions. Measured Sr and U values are thus several orders of magnitude higher than the detection limit, whereas some concentrations of Y and P are close to the detection limit. Variations in P, Sr, Y and U all exceed the relative uncertainties, and are therefore considered reliable. For more information on the method, accuracy and precision, the reader is referred to refs 32,35,36.

Dating and age–depth modelling. Twenty samples of speleothem GP2 were dated with the ^{230}Th/U-dating method (Supplementary Fig. 4). Measurements were conducted at the Helmholtz Centre for Ocean Research Kiel (GEOMAR), Germany, with an AXIOM MIC-ICP-MS (multiple ion counting inductively coupled plasma mass spectrometer). Aragonite contains high amounts of U, which resulted in a very precise age model (Supplementary Table 1 and Supplementary Fig. 4). All ages are presented using BP (AD 1950) as the datum. Further methodological details can be found in ref. 35. Age–depth modelling was performed with StalAge[36] (Supplementary Fig. 4). StalAge uses ensembles of three-point fits and, thus, attaches only little importance to individual ages in the border areas of the age model (that is, the top and bottom age of the speleothem). This may be reflected in considerably enlarged age model uncertainties in the border areas. To avoid this behaviour for the GP2 data set, we included two artificial data points with very large errors between the uppermost and lowermost data points (Supplementary Fig. 4 and Supplementary Table 1). We note that these two points do not contain additional age information, due to the associated large uncertainty.

Tuning of the Bunker Cave Mg/Ca record and calculations of the correlations. Because the GP2 record has a very precise chronology and small uncertainties, the Bunker Cave Mg/Ca record was tuned to the GP2 record (that is, the GP2 chronology was regarded as 'true', with negligible age uncertainties). For tuning, we adopted the approach of ref. 37 to obtain proxy time series with maximum correlation for both locations. The methods applied for interpolation are similar. However, in contrast to the approach used in ref. 37, we allow only one record to be shifted within its age uncertainties. To assess the significance of the obtained correlation, the same tuning approach was applied to 2000 artificially generated random time series with the same characteristics (that is, variance, auto-correlation coefficients, data resolution and absolute ages with according age uncertainties) as the real time series (in this case, the Bunker Cave Mg/Ca record). By tuning these 2000 artificial time series to the main record (GP2 δ^{18}O), a distribution of the maximum correlation coefficients is obtained. The tuning was then performed with the same procedure as for the measured time series. From the distribution of maximum correlation coefficients derived for the artificial data sets, the significance level of a correlation coefficient for the measured time series can be estimated. For example, if only 1% of the tuned artificial time series reach a correlation coefficient >0.7, a correlation coefficient >0.7 is significant at the 99% significance level. Please note that 'significance level' is defined slightly differently here than for the normally used *p*-value. Both records were smoothed with a time window of 50 years, which corresponds to the lowest sampling resolution of stalagmite GP2, where GP2 growth rate is the lowest.

From Bunker Cave we used two stalagmites for the tuning approach (Bu2 and Bu4)[6]. Bu2 covers the interval from 10.7 to 7.6 ka, whereas Bu4 covers the interval from 8.1 to 0 ka. A comparison of the non-tuned Bu2 and Bu4 Mg/Ca records with our GP2 δ^{18}O is shown in Supplementary Fig. 10. On the basis of this comparison, the Bu4 record was subdivided into three parts before tuning (8.1–5.9, 5.9–4.7, and 4.7–2.5 ka; Supplementary Fig. 10). The positive correlation obtained between the tuned Bu2 Mg/Ca and GP2 δ^{18}O record is mainly forced by the interval from 10.7 to 9.0 ka (Fig. 2 and Supplementary Table 2). The younger part (that is, after 9.0 ka) reduces the positive correlation because there is a tendency towards a negative correlation (see Supplementary Methods). Note that we tried to tune towards both positive and negative correlations for each tuned interval to show that it is only possible to obtain either a significant positive or negative correlation (Supplementary Table 2).

Climate modelling. We applied the Earth system model COSMOS to simulate time slices from the Holocene. COSMOS consists of three model compartments: the atmospheric circulation model ECHAM5[38], the dynamical vegetation model JSBACH[39,40], and the ocean general circulation model MPIOM[41]. COSMOS has been used for various palaeoclimate applications[16,17,42–44].

We applied six different experiments covering the late Holocene, mid-Holocene and early Holocene with prescribed orbital parameters (calculated after ref. 45 and greenhouse gases[46–48]):

(1) Pre-industrial control simulation (denoted as PI).
(2) Mid-Holocene (6k).
(3) Early Holocene (9k).
(4) Early Holocene including only the Laurentide ice sheet (9k.ice). The topography at 9 ka is based on a reconstruction from the ice-sheet model ICE-5G (VM2)[4]. This yields a ~17 m sea-level drop, which is smaller than those indicated by the proxy records (ref. 49 and references therein).
(5) Early Holocene including only the melt water perturbation (9k.melt). The North Atlantic fresh water inflow of 0.09 Sv has been distributed uniformly in the area of ice rafted detritus sedimentation, the so-called 'Ruddiman belt' between 40° N and 60° N (ref. 50).
(6) Early Holocene, including both the Laurentide ice sheet and its ice melt that lead to freshwater input into the North Atlantic (9k.comb).

The atmosphere results of all experiments have a spatial resolution of approximately 3.75° × 3.75° with 19 vertical levels (T31L19). Each of the

experiments is run to quasi-equilibrium (Supplementary Table 3). For additional information about the model set-up the reader is referred to ref. 17.

Calculation of the correlation patterns between SLP and precipitation. The correlation patterns are based on the 21-year running mean local precipitation time series from the location of Bunker Cave and Grotte de Piste and the SLP fields between 90° W–35° E and 25°–90° N. All data sets consist of 100-year-long winter mean (DJF) model results. Only values larger than the 95% confidence level are plotted.

Calculation of the canonical correlation analysis (CCA). The CCA method is applied to identify the strongest coupled SLP and SST patterns, which measures the linear relationship between these two multiple dependent variables[51]. To focus on the longer-timescale variation, that is, multi-decadal to centennial, all the data have been filtered with a 21-yr running mean after detrending. Only the two most strongly coupled pairs are shown here, with the SST and SLP resembling the NAO-like and AMO-like patterns, respectively. Different integration intervals for each experiment (Supplementary Table 3) result in the different data lengths used in CCA. Except for a period of 600 years in 9k.melt, at least 1,000-year data from each simulation have been taken into account for the CCA.

Calculation of AMO indices and AMO SLP anomalies. The AMO index is calculated by using the area-weighted mean from the North Atlantic monthly mean SSTs (0 to 60N and 285 to 352.5E). The time series were additionally detrended and smoothed with a 121-month smoother. For the calculation of the AMO SLP anomalies, the AMO indices were filtered by ±1 s.d.; SLP anomalies are expressed as AMO^+ SLP minus AMO^- SLP. For visualization, annual mean values are used.

Code availability. We are unable to make the computer code associated with this paper available because of its length and a signed contract with its main developers. The code and model data are available upon request.

Data availability. The stalagmite GP2 $\delta^{18}O$, $\delta^{13}C$ and trace element data, the stalagmites Bu2 and Bu4 tuned and normalized Mg/Ca data, and outside air temperature data from the Grotte de Piste site are available at https://www.ncdc.noaa.gov/paleo/study/20266. All other data are available upon request.

References

29. Kim, S. T., O'Neil, J. R., Hillaire-Marcel, C. & Mucci, A. Oxygen isotope fractionation between synthetic aragonite and water: influence of temperature and Mg^{2+} concentration. *Geochim. Cosmochim. Acta* **71,** 4704–4715 (2007).
30. Romanek, C. S., Grossman, E. L. & Morse, J. W. Carbon isotope fractionation in synthetic aragonite and calcite—effects of temperature and precipitation rate. *Geochim. Cosmochim. Acta* **56,** 419–430 (1992).
31. Finch, A. A., Shaw, P. A., Holmgren, K. & Lee-Thorp, J. Corroborated rainfall records from aragonitic stalagmites. *Earth Planet. Sci. Lett.* **215,** 265–273 (2003).
32. McMillan, E. A., Fairchild, I. J., Frisia, S., Borsato, A. & McDermott, F. Annual trace element cycles in calcite–aragonite speleothems: evidence of drought in the western Mediterranean 1200–1100 yr BP . *J. Quat. Sci.* **20,** 423–433 (2005).
33. Jochum, K. P., Stoll, B., Herwig, K. & Willbold, M. Validation of LA-ICP-MS trace element analysis of geological glasses using a new solid-state 193 nm Nd:YAG laser and matrix-matched calibration. *J. Anal. At. Spectrom.* **22,** 112–121 (2007).
34. Jochum, K. P. *et al*. Determination of reference values for NIST SRM 610–617 glasses following ISO guidelines. *Geostand. Geoanal. Res.* **35,** 397–429 (2011).
35. Fietzke, J., Liebetrau, V., Eisenhauer, A. & Dullo, C. Determination of uranium isotope ratios by multi-static MIC-ICP-MS: method and implementation for precise U- and Th-series isotope measurements. *J. Anal. At. Spectrom.* **20,** 395–401 (2005).
36. Scholz, D. & Hoffmann, D. L. StalAge—an algorithm designed for construction of speleothem age models. *Quat. Geochronol.* **6,** 369–382 (2011).
37. Fohlmeister, J. A statistical approach to construct composite climate records of dated archives. *Quat. Geochronol.* **14,** 48–56 (2012).
38. Roeckner, E. *et al*. *The Atmospheric General Circulation Model ECHAM5. Part 1: Model Description* Vol. 131 (Max Planck Institute for Meteorology, 2003).
39. Raddatz, T. J. *et al*. Will the tropical land biosphere dominate the climate-carbon cycle feedback during the twenty-first century? *Clim. Dynam.* **29,** 565–574 (2007).
40. Brovkin, V., Raddatz, T., Reick, C. H., Claussen, M. & Gayler, V. Global biogeophysical interactions between forest and climate. *Geophys. Res. Lett.* **36,** L07405 (2009).
41. Marsland, S. J., Haak, H., Jungclaus, J. H., Latif, M. & Roske, F. The Max-Planck-Institute global ocean/sea ice model with orthogonal curvilinear coordinates. *Ocean Model.* **5,** 91–127 (2003).
42. Stepanek, C. & Lohmann, G. Modelling mid-Pliocene climate with COSMOS. *Geosci. Model Dev.* **5,** 1221–1243 (2012).
43. Knorr, G., Butzin, M., Micheels, A. & Lohmann, G. A warm Miocene climate at low atmospheric CO_2 levels. *Geophys. Res. Lett.* **38,** L20701 (2011).
44. Wei, W., Lohmann, G. & Dima, M. Distinct modes of internal variability in the global meridional overturning circulation associated with the Southern Hemisphere westerly winds. *J. Phys. Oceanogr.* **42,** 785–801 (2012).
45. Berger, A. L. Long-term variations of daily insolation and Quaternary climatic changes. *J. Atmos. Sci.* **35,** 2362–2367 (1978).
46. Indermuhle, A. *et al*. Holocene carbon-cycle dynamics based on CO_2 trapped in ice at Taylor Dome, Antarctica. *Nature* **398,** 121–126 (1999).
47. Sowers, T., Alley, R. B. & Jubenville, J. Ice core records of atmospheric N_2O covering the last 106,000 years. *Science* **301,** 945–948 (2003).
48. Brook, E. J., Harder, S., Severinghaus, J., Steig, E. J. & Sucher, C. M. On the origin and timing of rapid changes in atmospheric methane during the last glacial period. *Glob. Biogeochem. Cycles* **14,** 559–572 (2000).
49. Carlson, A. E. & Clark, P. U. Ice sheet sources of sea level rise and freshwater discharge during the last deglaciation. *Rev. Geophys.* **50,** RG4007 (2012).
50. Ruddiman, W. F. Late Quaternary deposition of ice-rafted sand in subpolar North Atlantic (lat 40° to 65° N). *Geol. Soc. Am. Bull.* **88,** 1813–1827 (1977).
51. Dima, M. & Lohmann, G. A hemispheric mechanism for the Atlantic Multidecadal Oscillation. *J. Clim.* **20,** 2706–2719 (2007).